

1 A Pattern Search Based Inverse Method

Haiyan Zhou,¹ J. Jaime Gómez-Hernández¹ and Liangping Li¹

Haiyan Zhou, J. Jaime Gómez-Hernández and Liangping Li, Group of Hydrogeology, Department of hydraulics and environmental engineering, Universitat Politècnica de València, Camino de Vera, s/n 46022 Valencia, Spain. (haizh@upvnet.upv.es; zhouhaiyan2006@gmail.com)

¹Group of Hydrogeology, Department of hydraulics and environmental engineering, Universitat Politècnica de València, Valencia, Spain.

2 **Abstract.** Uncertainty of model predictions is caused to a large extent
3 by the uncertainty on model parameters while the identification of model pa-
4 rameters is demanding due to the inherent heterogeneity of the aquifer. A
5 variety of inverse methods has been proposed for parameter identification.
6 In this paper we present a novel inverse method to constrain the model pa-
7 rameters (hydraulic conductivities) to the observed state data (hydraulic heads).
8 In the method proposed we build a conditioning pattern consisting of sim-
9 ulated model parameters and observed flow data. The unknown parameter
10 values are simulated by pattern searching through an ensemble of realiza-
11 tions rather than optimizing an objective function. The model parameters
12 do not necessarily follow a multiGaussian distribution and the nonlinear re-
13 lationship between the parameter and the response is captured by the mul-
14 tipoint pattern matching. The algorithm is evaluated in two synthetic bimodal
15 aquifers. The proposed method is able to reproduce the main structure of
16 the reference fields and the performance of the updated model in predict-
17 ing flow and transport is improved compared with that of the prior model.

1. Introduction

18 The inverse problem in hydrogeology aims to gain understanding about the characteris-
19 tics of the subsurface, i.e., identification of model structure and corresponding parameters
20 by integrating observed model responses such as hydraulic head and mass concentration
21 data. Several inverse methods have been proposed to solve the inverse problem in the
22 last several decades. At the early stages of inverse modeling, a single “best” estimate of
23 hydraulic conductivities was pursued. Examples can be found in the works by *Kitanidis*
24 *and Vomvoris* [1983]; *Hoeksema and Kitanidis* [1984, 1985], who proposed the geostatistical
25 method to identify the parameters of the underlying variogram that describes the
26 multiGaussian random function used to characterize the spatial heterogeneity of hydraulic
27 conductivities; once these parameters were identified, the hydraulic conductivity map was
28 obtained by cokriging using the conductivity and piezometric head data. Another exam-
29 ple can be found in the work by *Carrera and Neuman* [1986], who treated the aquifer
30 properties as piecewise homogeneous. These approaches produced maps of conductivity
31 which were capable of reproducing the observed heads but which were too smooth to be
32 used for transport predictions, since they lacked the short scale variability observed in
33 the field. It was, thus, realized that the aquifer should be characterized by heterogeneous
34 distributions of the parameters [see *De Marsily et al.*, 2005, for a historic perspective
35 on the treatment of heterogeneity in aquifer modeling]. There are already several inverse
36 methods capable of dealing with this heterogeneity, e.g., the pilot point method [*RamaRao*
37 *et al.*, 1995], the self-calibration method [*Gómez-Hernández et al.*, 1997; *Wen et al.*, 1999;
38 *Hendricks Franssen et al.*, 2003], the ensemble Kalman filter [*Evensen*, 2003; *Chen and*

39 *Zhang, 2006; Hendricks Franssen and Kinzelbach, 2008; Zhou et al., 2011*] or the Markov
40 chain Monte Carlo method [*Oliver et al., 1997; Fu and Gómez-Hernández, 2009*].

41 In the above referred inverse methods, the groundwater model structure is described
42 by a variogram model, which basically measures the correlation between two spatial lo-
43 cations. This two-point variogram-based model is not able to characterize curvilinear
44 features, e.g., cross-bedded structures in fluvial deposits or erosion fractures in karstic
45 formations, while these curvilinear structures play a key role in flow and especially solute
46 migration modeling [e.g., *Kerrou et al., 2008; Li et al., 2011a*]. A solution to address this
47 issue is to use multiple-point geostatistics. A “training image”, which contains the types
48 of features to be reproduced by the aquifer model, is introduced as a geological conceptual
49 model [*Guardiano and Srivastava, 1993*]. This training image is used to derive experimen-
50 tal local conditional distributions that serve to propagate the curvilinear patterns onto
51 the simulated aquifer. Several programs based on multiple-point geostatistics are avail-
52 able, e.g., SNESIM [*Strebelle, 2002*], FILTERSIM [*Zhang et al., 2006*], SIMPAT [*Arpat*
53 *and Caers, 2007*] and DS [*Mariethoz et al., 2010a*], and a detailed review on multiple-
54 point geostatistics is provided by *Hu and Chuginova [2008]*. The advantages of using
55 multiple-point geostatistics for the characterization of hydraulic conductivity and for flow
56 and transport prediction have been confirmed after comparison with variogram-based sim-
57 ulation methods, both in synthetic examples and in real aquifers [e.g., *Feyen and Caers,*
58 *2006; Huysmans and Dassargues, 2009; Journel and Zhang, 2006*].

59 Most of the inverse methods construct an objective function to measure the deviation
60 between the simulated and observed data. Then, through an optimization algorithm,
61 the initial aquifer models are modified until the observed data are well reproduced by

62 the model predictions. However, during the optimization process, the aquifer spatial
63 structure may be modified with respect to the structure of the initial guesses and become
64 geologically unrealistic [Kitanidis, 2007]. To prevent this departure, techniques such as
65 including a regularization term or using a plausibility criterion are combined with the
66 objective function to constrain the deviation of the updated model from the prior model
67 [Alcolea et al., 2006; Emsellem and De Marsily, 1971; Neuman, 1973]. But these methods
68 have been challenged on their theoretical foundations [RamaRao et al., 1995; Rubin et al.,
69 2010]. Some recent inverse methods use other avenues in an attempt to preserve the prior
70 structure when perturbing the parameter values in the prior fields.

71 Considering the limits of the conventional inverse methods and the advantages of
72 multiple-point geostatistics, a reasonable solution is to use the multiple-point geostatistics
73 to characterize the nonlinear structure and to try to preserve this structure when
74 the model is updated using inverse methods. In this way, the curvilinear features are
75 characterized properly and the model remains physically realistic during the inverse process.
76 A few examples of such inverse methods include the gradual deformation method
77 (GDM) [Hu, 2000; Caers, 2003], the probability perturbation method (PPM) [Caers,
78 2002; Caers and Hoffman, 2006] and the probability conditioning method (PCM) [Jafarpour
79 and Khodabakhshi, 2011]. In all three methods, the prior model structure can
80 be characterized by multiple-point statistics and the property realizations are updated
81 in such a way that the prior model statistics are kept. The difference between the three
82 methods resides in the way the observations are integrated and the way the realizations
83 are updated. The main idea of the GDM is that the realizations are perturbed by modifying
84 the random number used to draw from the conditional distribution functions inherent

85 to the sequential simulation algorithm. This random number is chosen through optimiz-
86 ing a deformation parameter so that the mismatch between the simulated and observed
87 dynamic data is reduced. The PPM is based on modifying the conditional probability
88 functions themselves. For the case of PCM, the realizations are updated with a multiple-
89 point simulation method under a soft constraint given by a probability map inferred from
90 observed flow data. The probability map is built with the help of the ensemble Kalman
91 filter.

92 Alternatively to the inverse methods formulated in the framework of minimizing an
93 objective function, the Markov chain Monte Carlo method provides another way to tackle
94 the problem, namely, sampling from a posterior distribution that is already conditioned to
95 observations. Two such examples that are capable of dealing with curvilinear structures
96 are the blocking moving window algorithm [*Alcolea and Renard, 2010*] and the iterative
97 spatial resampling [*Mariethoz et al., 2010b*]. Another avenue is treating the inverse prob-
98 lem as a search problem, e.g., the distance-based inverse method proposed by *Suzuki and*
99 *Caers* [2008]. A large number of multiple-point simulations are constructed, from which
100 a search scheme is used to select those consistent with the observed dynamic data. The
101 spatial structure of the parameters is not disturbed since no modification is performed,
102 simply a selection is carried out. The updated model should be geologically realistic as
103 long as the prior model is so.

104 In this paper, we present a novel approach to constrain hydraulic conductivity realiza-
105 tions to dynamic flow data. The most distinct novelty of the proposed method is that
106 we formulate the inverse problem on the basis of pattern search instead of minimizing an
107 objective function or sampling the posterior distribution. We assume that the hydraulic

108 conductivity to be simulated is related to the geologic structure and to the flow dynam-
109 ics in its neighborhood. The value at each simulated cell is determined by searching
110 for matches, through an ensemble of realizations, to the conditional pattern composed
111 of simulated hydraulic conductivities and observed flow data. The proposed pixel-based
112 method is not only convenient to condition to local data but it is also able to capture the
113 geologic structure inherent to the initial seed realization. The pattern is searched through
114 an ensemble of realizations, all of which are consistent with the geologic structure, so that
115 the pattern-search method ensures that the updated fields are physically realistic and the
116 prior statistics are preserved.

117 The rest of the paper is organized as follows. In section 2, the proposed method is
118 presented in detail. In section 3, a synthetic example is described to assess the performance
119 of the method. In section 4, the results of the synthetic experiment are presented and
120 analyzed. In section 5, the method is further evaluated with another example to test the
121 effect of the number of conditioning data and of the boundary conditions. In section 6,
122 a few issues about the method are discussed. In section 7, some conclusions about the
123 proposed method are given.

2. Methodology

124 The method is based on the direct sampling algorithm proposed by *Mariethoz et al.*
125 [2010a]. It has been extended to include transient state observation data, which requires
126 the enlargement of the concept of training image to a training ensemble of realizations.
127 Also, in the same line as the ensemble Kalman filter approach, the ensemble of realizations
128 that serve as training image are updated as new sets of state observation data are collected.

2.1. Flow chart of the algorithm

129 A flow chart of the proposed method is displayed in Figure 1, which consists of the
130 following steps:

131 Step 1. Generate the prior ensemble of realizations. For the purpose of illustration we
132 will consider that hydraulic conductivity is the parameter of interest. Let the ensemble be
133 composed of N_r realizations and each hydraulic conductivity field be discretized into N_n
134 cells. Multiple-point sequential simulation methods are applied to generate the conduc-
135 tivity field ensemble, e.g., using the SNESIM or the DS codes mentioned in the previous
136 section. A training image is needed for the generation. This training image will not be
137 used again. At this initial stage, no observation state data are considered. The hydraulic
138 conductivity hard data are honored if available. Time is set to zero.

139 Loop on time t begins.

140 Step 2. Increase t to the next time step. Forecast the dependent state variables.
141 For each realization of the ensemble, the hydraulic head data for the current time t
142 are obtained by solving the transient flow equation, from time zero to time t , on the
143 hydraulic conductivity field subject to initial and boundary conditions. (We assume that
144 the initial and boundary conditions are known perfectly so that we can focus on the
145 uncertainty caused by hydraulic conductivities.) At this stage we have an ensemble of
146 hydraulic conductivity realizations that mimic the patterns of the training image, and
147 the corresponding ensemble of piezometric head fields. These two ensembles will become
148 now the training images in which to look for joint patterns of both conductivities and
149 piezometric heads that will permit the generation of a new set of conductivity realizations

150 consistent with the piezometric head measurements. Piezometric head data are observed,
151 and become conditioning data.

152 Loop on realizations begins.

153 Loop on cells begins.

154 Step 3. A new ensemble of realizations will be generated. For each realization, define
155 a random path visiting each cell except those with hydraulic conductivity measurements.
156 For each cell with an unknown value (K_i) in the random path,

157 • Step 3A. Determine the conditional data pattern of K_i . In this work, the data pat-
158 tern is composed of both hydraulic conductivities and piezometric heads. The conditional
159 hydraulic conductivities include measured hard data, if any, and previously simulated
160 values. A maximum number M of conditional hydraulic conductivities and a maximum
161 number N of conditional piezometric heads are set. Only the closest M hydraulic con-
162 ductivities and the closest N observed heads are stored as conditional data constituting
163 the conditioning pattern. For instance, in Figure 2, the conditioning data pattern for
164 K_i consists of three hydraulic conductivities and two observed heads. The size of the
165 conditional data pattern is not determined by a maximum search area but instead by
166 the number of conditioning data. The varying-size search neighborhood scheme was pro-
167 posed by *Mariethoz et al.* [2010a]. Advantages of this pattern configuration are two-fold:
168 (i) the size of the conductivity data event in the pattern is influenced by the density
169 of the known conductivities, i.e., when the known conductivities are sparse, the pattern
170 will cover a large area to reach the maximum number of conditioning data (M); on the
171 contrary, when the known conductivities are dense, the pattern will cover a small area
172 and only the nearest cells are used to account for the local variety. In other words, the

flexible search neighborhood scheme has similar effect as multiple-grids [Mariethoz *et al.*,
 2010a]; (ii) only hydraulic heads located near the unknown cell (N at most) are considered
 rather than all the heads over the field, which helps to avoid potential spurious correlation
 between simulated hydraulic conductivities and head observations.

- Step 3B. Given the conditional pattern, start a search in the ensemble of training image couples (hydraulic conductivity-piezometric head) for a match to the conditional pattern. Randomly start from a realization couple in the ensemble and then follow the ensemble sequentially. The search is not conducted on the entire realization, but it is restricted to a close neighborhood around the location of K_i , this restriction is enforced because hydraulic heads depend not only on hydraulic conductivities but also on the boundary conditions and the presence of sinks or sources. More specifically, in this work, we search only within a 3 by 3 square as shown in Figure 3, i.e., only 9 pattern candidates in a 3 by 3 square are evaluated in each realization. Calculate the distance function (d) between the conditioning data and the candidate:

$$d = \omega d_k + (1 - \omega) d_h \quad (1)$$

where d_k and d_h are the distances between the conditioning data and the candidate pattern corresponding to hydraulic conductivities and heads, respectively; ω is a trade-off coefficient used to balance the influence of the two types of conditioning data. This weight technique has been applied in many inverse methods and a usual choice for the value of ω is 0.5 when two types of conditioning data are taken into account and the distance measures are normalized [e.g., Alcolea and Renard, 2010; Capilla and Llopis-Albert, 2009; Christiansen *et al.*, 2011; Hendricks Franssen *et al.*, 2003]. The expression of the distance function will be discussed later on.

185 • Step 3C. Assign the value of K_i . If the distance function value d is less than a
186 predefined threshold (d_t), locate the value of K relative to the conditioning pattern in
187 the matching realization and assign it to K_i . If $d_t = 0$, the conditioning data are exactly
188 matched; if $d_t > 0$, a certain disagreement is allowed. To explicitly distinguish the misfits
189 related with hydraulic conductivities and heads in the conditioning data pattern, we can
190 define two thresholds, $d_{t,k}$ and $d_{t,h}$. In the present work, hydraulic conductivities are
191 considered as categorical variables (two facies with uniform values) and the corresponding
192 $d_{t,k}$ is set to 0, indicating an exact fit. Normally $d_{t,h}$ is assigned a value larger than 0 to
193 account for measurement errors and the difficulty of fitting exactly a continuous variable
194 (a value of $d_{t,h} = 0.005$ was used, after some trial, in the examples following). If no match
195 is found with distances below the predefined thresholds, the pattern with the smallest
196 distance is used.

197 Loop back to step 3A for generation of the next cell until all cells for the current
198 realization are visited.

199 Loop back to step 3 to start the generation of the next realization until all realizations
200 are generated.

201 Step 4. Postprocessing. Inconsistencies may appear during data assimilation as shown
202 in Figure 4. We can find that the cells indicated by the ellipses are not consistent with
203 their neighboring values, and cannot be considered geologically realistic. We simply filter
204 these inconsistent values out similarly as *Henrion et al.* [2010] did. However, this might
205 disturb the facies proportions since no proportion control strategy is applied. In order
206 to reduce the influence of the artificial filtering on facies proportion, we only consider
207 those inconsistent objects consisting of at most three cells. More complex postprocessing

208 methods can be found in image processing algorithms, e.g., kernel principal component
 209 analysis [*Kim et al.*, 2005; *Mika et al.*, 1999], or others [*Falivene et al.*, 2009].

210 Step 5. Update the training images. The set of conductivity realizations generated
 211 become the new set of training images.

212 Loop back to step 2 for the next time step until all transient hydraulic heads have been
 213 used.

2.2. Distance function

In the proposed method, the distance function plays a key role and it must be defined carefully. The Minkowski distance is a commonly used distance function as defined below [*Borg and Groenen*, 2005; *Duda et al.*, 2001].

$$d\{d(x_n), p(x_n)\} = \left(\sum_{i=1}^n |d(x_i) - p(x_i)|^q \right)^{1/q} \quad (q \geq 1) \quad (2)$$

214 where $d\{d(x_n), p(x_n)\}$ is the distance function between the data event $d(x_n)$ and the
 215 conditioning data pattern $p(x_n)$, n indicates the size of $d(x_n)$ and $p(x_n)$, x can be hydraulic
 216 conductivity and head data, and q is a variable that, if equal to 1, gives rise to the
 217 Manhattan distance, and if it is equal to 2, to the Euclidian distance.

218 1. Manhattan distance (city-block distance) has been used as the dissimilarity measure
 219 in SIMPAT, a multiple-point geostatistical simulation algorithm [*Arpat and Caers*, 2007].

- Categorical variables:

$$d\{d(x_n), p(x_n)\} = \frac{1}{n} \sum_{i=1}^n a_i \quad d \in [0, 1] \quad (3)$$

$$a_i = \begin{cases} 0, & \text{if } d(x_i) = p(x_i) \\ 1, & \text{otherwise} \end{cases}$$

220 The distance values are normalized into the range $[0, 1]$ by dividing by n , which makes it
 221 convenient to define the threshold values, i.e., threshold values near 0 indicate very low

222 deviation and near 1 very high deviation. It also helps in combining the distances for
 223 different attributes.

- Continuous variables:

$$d\{d(x_n), p(x_n)\} = \frac{1}{n} \sum_{i=1}^n \frac{|d(x_i) - p(x_i)|}{d_{max}} \quad d \in [0, 1] \quad (4)$$

224 where d_{max} is the maximum deviation between $d(x_i)$ and $p(x_i)$, together with n used to
 225 normalize the distance values.

226 2. Weighted Euclidean distance attributes different weights to elements in the data
 227 event depending on their distance to the simulated cell, i.e., the nearer to the simulated
 228 cell, the more important, while in the unweighted Manhattan distance, all elements share
 229 the same weight.

- Categorical variables:

$$d\{d(x_n), p(x_n)\} = \frac{1}{\sum_{i=1}^n h_i^{-1}} \sum_{i=1}^n a_i h_i^{-1} \quad d \in [0, 1] \quad (5)$$

230 where h_i is the lag distance from the element in the data event to the simulated cell and
 231 a_i is the same as in Equation 3.

- Continuous variables:

$$d\{d(x_n), p(x_n)\} = \left(\frac{1}{\sum_{i=1}^n h_i^{-1}} \sum_{i=1}^n \frac{|d(x_i) - p(x_i)|^2 h_i^{-1}}{d_{max}^2} \right)^{1/2} \quad d \in [0, 1] \quad (6)$$

232 where d_{max} is the same as in Equation 4 and h_i is the same as in Equation 5.

233 The Manhattan distance and the weighted Euclidian distance functions defined above
 234 were first proposed in developing the DS [*Mariethoz et al.*, 2010a] and then modified in
 235 this work. Manhattan distance functions (Equations 3 and 4) are more computationally
 236 efficient than Euclidian ones (Equations 5 and 6). An alternative to the Minkowski-based

237 distance family is the Hausdorff distance [*Dubuisson and Jain, 1994*], which has been
238 used, for instance, by *Suzuki and Caers* [2008].

3. Synthetic example A

239 A synthetic experiment is designed to evaluate the performance of the proposed method.
240 The test aquifer is assumed confined and it covers a domain discretized into $100 \times 80 \times 1$
241 cells, with cell dimensions of $1 \text{ m} \times 1 \text{ m} \times 10 \text{ m}$. A training image for the facies (Figure
242 5) was generated using the object-based geologic modeling program FLUVSIM [*Deutsch*
243 *and Tran, 2002*]. This training image serves as a conceptual model of the bimodal aquifer
244 composed of high permeability sand and low permeability shale. Uniform permeability
245 values are assigned to the two facies, i.e., $\ln K = -4 \text{ m/d}$ for the shale and $\ln K = 1 \text{ m/d}$
246 for the sand. DS [*Mariethoz et al., 2010a*], a pattern-based multiple-point geostatistical
247 simulation algorithm, is used to generate the reference facies field (Figure 6) by borrow-
248 ing structures from the training image. Hydraulic conductivities at 20 locations in the
249 reference are collected serving as the conditioning hard data (see Figure 6 for locations of
250 the measurements).

251 MODFLOW2000 [*Harbaugh et al., 2000*], a finite-difference flow simulator, is used to
252 solve the transient groundwater flow equation on the reference field subject to the bound-
253 ary conditions: impermeable boundaries in the north and south, constant head in the
254 west ($H = 0 \text{ m}$) and prescribed flow rate in the east ($Q = 100 \text{ m}^3/\text{d}$). Notice that the flow
255 pumping rates in the east boundaries are not uniform, but proportional to the conduc-
256 tivities at the boundary. The initial head is 0 m everywhere over the field. A simulation
257 period of 30 days is discretized into 20 time steps following a geometric sequence of ratio
258 1.05. Specific storage is assumed constant and equal to 0.003 m^{-1} . Piezometric head data

259 at 63 observation locations are collected serving as the conditioning data to update the
260 prior model parameters. Configuration of the 63 piezometers is shown in Figure 6.

261 The number of conditioning data (20 hydraulic conductivity values, and 63 piezometric
262 head time series) maybe unrealistically large for practical situations, although it may not
263 be in controlled experiments. Example B below uses a reduced number of conditioning
264 data. The main purpose of this example is to test the method in an extreme case with
265 lots of state conditioning data. The larger the number of state conditioning data, the
266 more stress is put on the inverse algorithm to find acceptable solutions.

267 The prior ensemble of realizations consists of 500 realizations which are generated by
268 DS using the same training image used to generate the reference (the reference field is,
269 of course, not a member of the initial ensemble of realizations). The 20 conductivity
270 hard data are honored when the prior realizations are generated. The prior ensemble
271 is generated so that the uncertainties related with the conceptual model and hydraulic
272 conductivity measurement are not considered in this experiment.

273 The observed piezometric heads in the first 6 time steps (6.17 days) are used to up-
274 date the prior realizations with the proposed method. The results after integrating the
275 observations are presented and discussed in the following section.

4. Results and discussions

4.1. Hydraulic conductivity characterization

276 Figure 7 shows the first four realizations in the ensemble before and after the head
277 data are assimilated. The prior realizations (left column) are conditioned to 20 hydraulic
278 conductivity measurements and the updated realizations (right column) are consistent
279 with both measured conductivity and observed piezometric head data. We can find that

280 the prior realizations deviate considerably from the reference field while the updated
 281 realizations resemble closely the reference. In other words, the main channel pattern is
 282 captured after integrating the observed piezometric heads. However, we notice that the
 283 updated realizations exhibit a little higher variability near the west boundaries than in the
 284 east (indicated by the three ellipses in the reference field). This can be attributed partly
 285 to the boundary conditions, since piezometric heads around prescribed head boundaries
 286 are not sensitive to hydraulic conductivity fluctuations.

Figure 8 summarizes the prior and posterior statistic metrics of $\ln K$ over the ensemble of realizations. The ensemble average (the second row of Figure 8, “EA”) of the prior realizations exhibits no channel trend while the updated EA shows clear channels and resembles the reference field. The ensemble standard deviation (the third row of Figure 8, “Std. dev.”) shows a significant reduction of uncertainty, i.e., in the prior model the uncertainties around the hard data are small and the uncertainties grow big when far away from the hard data locations while in the updated case they are reduced everywhere. We also plot the $RMSE$ (the bottom row of Figure 8) taking advantage of knowing the reference field exactly. The $RMSE(x)_i$ at a cell i is computed as

$$RMSE(x)_i = \left[\frac{1}{N_r} \sum_{j=1}^{N_r} (x_{i,j}^{sim} - x_i^{ref})^2 \right]^{1/2} \quad (7)$$

287 where N_r is the number of realizations in the ensemble, x can be either the $\ln K$ or the
 288 hydraulic head h , the superscripts sim and ref indicate simulation and reference model,
 289 respectively. Similarly with the standard deviation, the $RMSE(\ln K)$ field confirms the
 290 importance of assimilating observed piezometric head data in characterizing the structure
 291 of hydraulic conductivity. The error is clearly reduced in the updated ensemble compared
 292 with the prior case. Moreover, we calculate the average $RMSE(\ln K)$ over the field and

293 it is reduced from 3.0 m/d in the prior model to 1.5 m/d in the updated model. As we
294 have mentioned previously, the structure identification near the west boundaries is less
295 improved compared with the east part (separated by the dashed line) due to the influence
296 of the prescribed head boundaries.

4.2. Prediction capability of the updated model

297 To evaluate the prediction capacity of the updated model, we will use it to forecast
298 piezometric head evolution and mass transport. The initial and boundary conditions
299 remain the same as during the model calibration. Figure 9 shows the evolution of hydraulic
300 head with time in the simulation period (30 days) at two of the piezometers, where the left
301 column shows predictions with the prior model and the right column shows predictions
302 with the updated model after conditioning on the observed hydraulic head data until
303 6.17 days. The prediction uncertainty is substantially reduced in the updated $\ln K$ model
304 compared with the prior model. The average $RMSE(h)$ at each time step over the
305 hydraulic field is calculated and shown in Figure 10. We can argue that the hydraulic
306 head prediction with the updated model is improved not only at the observation locations
307 but over the whole field. Figure 11 summarizes the ensemble average, standard deviation
308 and $RMSE$ of the flow prediction at the end of the simulation with the prior and calibrated
309 model, separately.

310 Figure 12 illustrates the configuration of the transport prediction experiment. Con-
311 servative particles are released linearly along $x = 10$ m and three control planes across
312 the field are placed to record the arrival times of the particles. The random walk par-
313 ticle tracking program RW3D [Fernàndez-Garcia et al., 2005; Salamon et al., 2006; Li
314 et al., 2011b] is used to solve the transport equation in the $\ln K$ fields once the flow has

315 reached steady state. Advection and dispersion are both considered, with longitudinal
316 and transverse dispersivities of 0.5 m and 0.05 m, respectively. The porosity is assumed
317 constant as 0.3. Figure 13 shows the breakthrough curves (BTCs) at the three planes for
318 the prior ensemble (left column) and for the updated ensemble (right column). We can
319 see that the updated model reproduces the reference BTCs better than the prior model
320 does, i.e., the median of the travel times in the updated model resembles the reference
321 BTCs. Moreover, the prediction uncertainties measured by the 5th and 95th percentiles
322 are significantly reduced, i.e., the confidence interval is narrower, after the hydraulic heads
323 are conditioned.

5. Synthetic example B

5.1. Reference

324 In the previous synthetic example there are 20 hard conductivity data and 63 piezome-
325 ters used to calibrate the prior model. To further examine the performance of the proposed
326 method we test another application in a more realistic example where the observations are
327 available at only 9 locations. The inclusion of a pumping well in the center of the domain
328 also allows to investigate the method under a different flow configuration. This example
329 is similar to the one in *Alcolea and Renard* [2010] with respect to the conditioning hard
330 data, hydraulic head piezometers and boundary conditions.

331 The research domain of 100 m \times 100 m \times 10 m is discretized into 100 \times 100 \times 1 cells.
332 The reference field is generated with the multiple point geostatistical simulation algorithm
333 SNESIM [*Strebelle*, 2002] using the training image in Figure 14A. The reference field is
334 shown in Figure 14B, where the hydraulic conductivities are assumed constant within each
335 facies, i.e., $K = 10$ m/d for sand and $K = 10^{-3}$ m/d for shale. The transient flow equation

336 is solved on the reference confined aquifer under the boundary conditions: prescribed head
337 boundaries in the west ($H = 1$ m) and in the east ($H = 0$ m) and impermeable boundaries
338 in the north and south. A pumping well with a production of $100 \text{ m}^3/\text{d}$ is located at well
339 9 in Figure 14B. The initial head is 0 m over the field. The simulation period of 30 days
340 is discretized into 20 time steps following a geometric sequence of ratio 1.2.

5.2. Prior model and conditioning data

341 The prior model ensemble consists of 500 realizations which are generated with the same
342 algorithm (SNESIM) and the same training image (Figure 14A). This ensemble does not
343 include the reference field. Each realization is conditioned to the lithofacies measured from
344 the reference field at the 9 wells (Figure 14B), 6 of which are in sand the the other 3 are in
345 shale. The location of the conditioning wells does not correspond to a random sampling,
346 but it implicitly assumes that there is a priori geological/geophysical information that
347 helps drilling most of the wells in highly conductive zones. The head dynamics at the 9
348 wells in the reference field are collected for the first 10 time steps (4.17 days) and used as
349 conditioning data. The resulting model will be evaluated from facies recognition and flow
350 prediction capacity.

5.3. Calibrated model

5.3.1. Facies recognition

351
352 Figure 15 summarizes the reproduction of the facies by the conditional realizations. On
353 the first row a single realization is shown. It can be seen how, after updating, the channel
354 location is much closer to the one in the reference, the main channel features around the
355 conditioning wells are reproduced; however they fail to match the entire length of the
356 isolated branch towards the bottom of the reference, and the branch on the upper right

357 corner. In both cases the difficulty to identify these two channel branches has to do with
358 the small sensitivity that conductivity at these locations has with respect to piezometric
359 heads. Notice that both unidentified areas are connected to the no flow boundaries in one
360 of their extremes, so the flow channeling effect, particularly for the branch in the upper
361 right corner, does not exist. (This latter fact can better be noticed in Figure 16.) The
362 second row in Figure 15 shows the probability that a given cell is in sand, and the third
363 row, the ensemble variance map. When analyzing these last two maps, it is noticeable the
364 improvement that incorporating the piezometric head data brings to the characterization
365 of the hydraulic conductivity field. It is clear that the characterization is best for the
366 channels which are most affected by the presence of the pumping well. It is also clear
367 that if no wells had been located in the channels, their identification would have been less
368 precise. The largest uncertainties after updating are next to the left boundary, again due
369 to the lack of sensitivity of the hydraulic conductivities to the piezometric heads next to
370 prescribed head boundaries.

371 **5.3.2. Flow prediction**

372 Regarding flow predictions beyond the conditioning period, Figure 16 shows the flow
373 prediction at the end of simulation period (30 days) in one realization of the ensemble,
374 and Figure 17 displays the head evolution at the 9 wells in the prior and updated model.
375 From Figure 16 we can reach similar conclusions as when analyzing the characterization
376 of the conductivities, the updated model does quite a good job except for the part of
377 the channel branch towards the bottom that the conditioning model is not capable of
378 capturing. Figure 17 shows the head evolution up to and past the conditioning period in
379 all the 500 realizations before and after updating. We can appreciate the large reduction on

380 the spread of the piezometric head evolution in the different realizations. Analyzing each
381 well individually, we notice that piezometric head assimilation allows setting the barriers
382 that prevent the effect of the pumping to reach wells 7 and 8; well 1 still displays too much
383 fluctuation in the updated model, this is due to the difficulty of the updating algorithm to
384 capture the blob of shale which is in the reference field between wells 1 and 9, this failure
385 to capture such a feature may be due to the fact that such a feature is not too recurrent in
386 the training image and therefore it does not replicate often in the 500 realizations; wells 2,
387 3 and 4 are much better reproduced since the main channel branches connecting them to
388 well 9 are present; well 5 evolution is related to its connection to the prescribed west head
389 boundary and to the large shale barrier between the well 5 and the pumping well 9, the
390 reproduction of these two features in the updated fields produces such a good reproduction
391 for well 5; well 6 is very well reproduced during the conditioning period, but afterwards
392 the drawdowns are larger than observed, probably if the conditioning period had been
393 larger, better results could have been obtained; finally, well 9, the one with the largest
394 drawdowns reduces substantially its fluctuations with regard to the initial realizations, but
395 the conditioning is not as good as in the rest of the wells in absolute terms. The difficulty
396 to match better well 9 is related to the very large variability on the drawdowns at well
397 9 in the seed realizations; trying to find close matches to the conditional patterns when
398 generating the conductivity values for the nodes around the pumping well is particularly
399 difficult for the initial time steps, because the initial seed conductivities can have quite
400 different pattern structure, and therefore, quite heterogeneous piezometric heads around
401 the pumping well.

6. Discussion

402 The method we have presented takes advantage of the latest developments on multiple
403 point geostatistics and presents what we believe is a conceptually completely new approach
404 to inverse modeling in hydrogeology. While the method has been demonstrated to work
405 in two quite different experimental setups, there remain a number of issues that should
406 be further investigated in the future, such as:

- 407 • How to handle continuous hydraulic conductivities. The main attractiveness of the
408 DS simulation is that it can handle easily continuous distributions of the parameters
409 being simulated; however, in our first attempts of implementing the inverse pattern-search
410 algorithm using continuous hydraulic conductivities, it was always too difficult to find close
411 enough matching patterns to the conditional one, resulting, at the end, in too noisy images.
412 For this reason, we resorted back to the binary definition of the hydraulic conductivity
413 field to ease the finding of the matching patterns. The inverse pattern-search algorithm
414 should work with continuous conductivities but there is a need to explore the impact of
415 the size of the ensemble of realizations, to optimize the searching strategy and to come
416 up with good postprocessing algorithms that filter out the noise that appears in the final
417 realizations.

- 418 • Fine tune the distance functions. Which distance function to use when comparing
419 patterns to the conditioning one was already an issue in the DS algorithm. This issue
420 is augmented when the simulation is multivariate and two different variables have to be
421 considered. Each variable will have its own distance, how should these two distances be
422 combined? Should they be equally weighted? Should the Euclidean distance from the
423 cells in the pattern to the cell being simulated be considered in computing the distance

424 between patterns? Which should the acceptance thresholds be? These are questions
425 that require further analysis. In our case, we ended with an equal weight for both the
426 normalized conductivity distance and the normalized piezometric head distance, and we
427 used a threshold equal to zero for the conductivities, and a threshold of 0.005 for the heads;
428 in the latter case, we had to do some trial-and-error analysis, since when the threshold
429 was too small, it was difficult to find any match, but if it was too high, the matches were
430 not too good, and noise was apparent in the realizations.

431 • Sample space represented by the final ensemble of realizations. At this point, it is
432 difficult to make any assertion on whether the final ensemble of realizations spans a space
433 of uncertainty similar to the one that would be obtained by, for instance, sampling from
434 a posterior distribution by a Markov chain Monte-Carlo algorithm.

7. Summary and conclusions

435 We present a novel inverse method in this paper to estimate model parameters by
436 assimilating the observed flow data. The proposed method aims at recognizing the spatial
437 heterogeneity of the nonGaussian distributed model parameters while guaranteeing the
438 flow responses consistent with the observations. The model parameters are characterized
439 by multiple-point geostatistics what not only relaxes the assumption that the parameters
440 follow a Gaussian distribution but also is able to characterize complex curvilinear geologic
441 structures. The inverse method is based on the Direct Sampling of *Mariethoz et al.*
442 [2010a] and it is formulated on the basis of pattern searching, i.e., search an ensemble
443 of realizations for a data set which matches the conditional pattern composed of model
444 parameters and observations. A distance function is introduced to measure the misfit
445 between the conditional pattern and candidates. The searching scheme avoids the need

446 to use any optimization approach, and therefore, the danger of falling onto local minima.
447 Another advantage of the proposed method is that it is not only easy to condition to hard
448 data, since it is a pixel-based method, but it also capable of describing complex geologic
449 features while preserving a prior random function model.

450 The performance of the proposed method is assessed by two synthetic experiments in
451 an aquifer composed of two facies, sand and shale with contrasting hydraulic conductivity
452 values. The prior hydraulic conductivity models are updated by integrating observed
453 piezometric head data using the proposed method. The main channel structures in the
454 reference field are found to be well reproduced by the updated models. Furthermore, the
455 prediction capacity of the updated models are evaluated in flow and transport simulations,
456 for which both prediction error and uncertainty are significantly reduced.

457 **Acknowledgments.** The authors gratefully acknowledge the financial support by Min-
458 istry of Science and Innovation project CGL2011-23295. The first author also acknowl-
459 edges the scholarship provided by China Scholarship Council (CSC No. [2007] 3020). The
460 authors would like to thank Grégoire Mariethoz (The University of New South Wales)
461 and Philippe Renard (University of Neuchâtel) for their enthusiastic help in answering
462 questions about the Direct Sampling algorithm. Grégoire Mariethoz and two anonymous
463 reviewers are also thanked for their comments during the reviewing process, which helped
464 improving the final manuscript.

References

465 Alcolea, A., and P. Renard (2010), Blocking Moving Window algorithm: Condition-
466 ing multiple-point simulations to hydrogeological data, *Water Resources Research*, 46,

467 W08511, doi:10.1029/2009WR007943.

468 Alcolea, A., J. Carrera, and A. Medina (2006), Pilot points method incorporating prior
469 information for solving the groundwater flow inverse problem, *Advances in Water Re-*
470 *sources*, 29(11), 1678–1689.

471 Arpat, G. B., and J. Caers (2007), Conditional simulation with patterns, *Mathematical*
472 *Geology*, 39(2), 177–203, doi:10.1007/s11004-006-9075-3.

473 Borg, I., and P. J. Groenen (2005), *Modern multi-dimensioal scaling: Theory and appli-*
474 *cation*, 2nd edn., Springer., New York.

475 Caers, J. (2002), Geostatistical history matching under training-image based geological
476 model constraints, *SPE Annual Technical Conference and Exhibition*., SPE 77429.

477 Caers, J. (2003), Efficient gradual deformation using a streamline-based proxy method,
478 *Journal of Petroleum Science and Engineering*, 39(1-2), 57–83, doi:10.1016/S0920-
479 4105(03)00040-8.

480 Caers, J., and T. Hoffman (2006), The probability perturbation method: A new look at
481 bayesian inverse modeling, *Mathematical Geology*, 38(1), 81–100, doi:10.1007/s11004-
482 005-9005-9.

483 Capilla, J., and C. Llopis-Albert (2009), Gradual conditioning of non-Gaussian transmis-
484 sivity fields to flow and mass transport data: 1. Theory, *Journal of Hydrology*, 371(1-4),
485 66–74, doi:10.1016/j.jhydrol.2009.03.015.

486 Carrera, J., and S. P. Neuman (1986), Estimation of aquifer parameters under transient
487 and steady state conditions: 1. Maximum likelihood method incorporating prior infor-
488 mation, *Water Resources Research*, 22(2), 199–210.

- 489 Chen, Y., and D. Zhang (2006), Data assimilation for transient flow in geologic for-
490 mations via ensemble Kalman filter, *Advances in Water Resources*, 29(8), 1107–1122,
491 doi:10.1016/j.advwatres.2005.09.007.
- 492 Christiansen, L., P. J. Binning, D. Rosbjerg, O. B. Andersen, and P. Bauer-Gottwein
493 (2011), Using time-lapse gravity for groundwater model calibration: An application to
494 alluvial aquifer storage, *Water Resources Research*, doi:10.1029/2010WR009859.
- 495 De Marsily, G., F. Delay, J. Gonçalves, P. Renard, V. Teles, and S. Violette (2005), Dealing
496 with spatial heterogeneity, *Hydrogeology Journal*, 13(1), 161–183, doi:10.1007/s10040-
497 004-0432-3.
- 498 Deutsch, C., and T. Tran (2002), FLUVSIM: a program for object-based stochastic mod-
499 eling of fluvial depositional systems, *Computers & Geosciences*, 28(4), 525–535, doi:
500 10.1016/S0098-3004(01)00075-9.
- 501 Dubuisson, M.-P., and A. K. Jain (1994), A modified Hausdorff distance for object match-
502 ing, in *International conference on pattern recognition*, pp. 566–568, Jerusalem, Israel.
- 503 Duda, R. O., P. E. Hart, and D. G. Stork (2001), *Pattern classification, 2nd edn.*, John
504 Wiley & Sons.
- 505 Emsellem, Y., and G. De Marsily (1971), An automatic solution for the inverse problem,
506 *Water Resources Research*, 7(5), 1264–1283.
- 507 Evensen, G. (2003), The Ensemble Kalman Filter: Theoretical formulation and practical
508 implementation, *Ocean dynamics*, 53(4), 343–367, doi:10.1007/s10236-003-0036-9.
- 509 Falivene, O., P. Cabello, P. Arbués, J. A. Muñoz, and L. Cabrera (2009), A geostatistical
510 algorithm to reproduce lateral gradual facies transitions: Description and implementa-
511 tion, *Computers & Geosciences*, 35(8), 1642–1651, doi:10.1016/j.cageo.2008.12.003.

- 512 Fernàndez-Garcia, D., T. Illangasekare, and H. Rajaram (2005), Differences in the scale
513 dependence of dispersivity and retardation factors estimated from forced-gradient and
514 uniform flow tracer tests in three-dimensional physically and chemically heterogeneous
515 porous media, *Water Resources Research*, *41*(3), W03012, doi:10.1029/2004WR003125.
- 516 Feyen, L., and J. Caers (2006), Quantifying geological uncertainty for flow and trans-
517 port modeling in multi-modal heterogeneous formations, *Advances in Water Resources*,
518 *29*(6), 912–929, doi:10.1016/j.advwatres.2005.08.002.
- 519 Fu, J., and J. J. Gómez-Hernández (2009), A blocking Markov chain Monte Carlo method
520 for inverse stochastic hydrogeological modeling, *Mathematical Geosciences*, *41*(2), 105–
521 128, doi:10.1007/s11004-008-9206-0.
- 522 Gómez-Hernández, J. J., A. Sahuquillo, and J. E. Capilla (1997), Stochastic simulation of
523 transmissivity fields conditional to both transmissivity and piezometric data—I. Theory,
524 *Journal of Hydrology*, *203*(1-4), 162–174.
- 525 Guardiano, F., and R. Srivastava (1993), Multivariate geostatistics: beyond bivariate
526 moments, in *Geostatistics-Troia*, edited by A. Soares, pp. 133–144, Kluwer Academic
527 Publ, Dordrecht.
- 528 Harbaugh, A. W., E. R. Banta, M. C. Hill, and M. G. McDonald (2000), MODFLOW-
529 2000, the U.S. geological survey modular ground-water model — user guide to modular-
530 ization concepts and the ground-water flow process, *Tech. Rep. Open-File Report 00-92*,
531 U.S. Department of the Interior, U.S. Geological Survey, Reston, Virginia, 121pp.
- 532 Hendricks Franssen, H. J., and W. Kinzelbach (2008), Real-time groundwater flow mod-
533 eling with the Ensemble Kalman Filter: Joint estimation for states and parame-
534 ters and the filter inbreeding problem, *Water Resources Research*, *44*, W09408, doi:

- 535 10.1029/2007WR006505.
- 536 Hendricks Franssen, H. J., J. J. Gómez-Hernández, and A. Sahuquillo (2003), Coupled in-
537 verse modelling of groundwater flow and mass transport and the worth of concentration
538 data, *Journal of Hydrology*, *281*(4), 281–295, doi:10.1016/S0022-1694(03)00191-4.
- 539 Henrion, V., G. Caumon, and N. Cherpeau (2010), ODSIM: An Object-Distance Simula-
540 tion Method for Conditioning Complex Natural Structures, *Mathematical Geosciences*,
541 *42*(8), 911–924, doi:10.1007/s11004-010-9299-0.
- 542 Hoeksema, R. J., and P. K. Kitanidis (1984), An application of the geostatistical approach
543 to the inverse problem in two-dimensional groundwater modeling, *Water Resources*
544 *Research*, *20*(7), 1003–1020.
- 545 Hoeksema, R. J., and P. K. Kitanidis (1985), Analysis of the spatial structure of properties
546 of selected aquifers, *Water Resources Research*, *21*(4), 563–572.
- 547 Hu, L. Y. (2000), Gradual deformation and iterative calibration of Gaussian-related
548 stochastic models, *Mathematical Geology*, *32*(1), 87–108.
- 549 Hu, L. Y., and T. Chugunova (2008), Multiple-point geostatistics for modeling subsurface
550 heterogeneity: A comprehensive review, *Water Resources Research*, *44*(11), W11413,
551 doi:10.1029/2008WR006993.
- 552 Huysmans, M., and A. Dassargues (2009), Application of multiple-point geostatistics on
553 modelling groundwater flow and transport in a cross-bedded aquifer (Belgium), *Hydro-*
554 *geology Journal*, *17*(8), 1901–1911, doi:10.1007/s10040-009-0495-2.
- 555 Jafarpour, B., and M. Khodabakhshi (2011), A probability conditioning method (PCM)
556 for nonlinear flow data integration into multipoint statistical facies simulation, *Mathe-*
557 *matical Geosciences*, *43*(2), 133–164, doi:10.1007/s11004-011-9316-y.

- 558 Journal, A., and T. Zhang (2006), The necessity of a multiple-point prior model, *Mathe-*
559 *matical geology*, *38*(5), 591–610, doi:10.1007/s11004-006-9031-2.
- 560 Kerrou, J., P. Renard, H. J. Hendricks Franssen, and I. Lunati (2008), Issues in character-
561 izing heterogeneity and connectivity in non-multiGaussian media, *Advances in Water*
562 *Resources*, *31*(1), 147–159, doi:10.1016/j.advwatres.2007.07.002.
- 563 Kim, K. I., M. O. Franz, and B. Schölkopf (2005), Iterative kernel principal component
564 analysis for image modeling, *IEEE Transactions on Pattern Analysis and Machine In-*
565 *telligence*, *27*(9), 1351–1366, doi:10.1109/TPAMI.2005.181.
- 566 Kitanidis, P. K. (2007), On stochastic inverse modeling, in *Subsurface hydrology: Data*
567 *integration for properties and processes*, edited by D. W. Hyndman, F. D. Day-Lewis,
568 and K. Singha, pp. 19–30, American Geophysical Union, Washington, DC.
- 569 Kitanidis, P. K., and E. G. Vomvoris (1983), A geostatistical approach to the inverse
570 problem in groundwater modeling (steady state) and one-dimensional simulations, *Wa-*
571 *ter Resources Research*, *19*(3), 677–690.
- 572 Li, L., H. Zhou, H. J. Hendricks Franssen, and J. J. Gómez-Hernández (2011a), Ground-
573 water flow inverse modeling in non-multigaussian media: performance assessment of the
574 normal-score ensemble kalman filter, *Hydrology and Earth System Sciences Discussions*,
575 *8*(4), 6749–6788, doi:10.5194/hessd-8-6749-2011.
- 576 Li, L., H. Zhou, and J. J. Gómez-Hernández (2011b), Transport upscaling using multi-
577 rate mass transfer in three-dimensional highly heterogeneous porous media, *Advances*
578 *in Water Resources*, *34*(4), 478–489, doi:10.1016/j.advwatres.2011.01.001.
- 579 Mariethoz, G., P. Renard, and J. Straubhaar (2010a), The direct sampling method to per-
580 form multiple-point geostatistical simulaitons, *Water Resources Research*, *46*, W11536,

581 doi:10.1029/2008WR007621.

582 Mariethoz, G., P. Renard, and J. Caers (2010b), Bayesian inverse problem and optimiza-
583 tion with iterative spatial resampling, *Water Resources Research*, *46*(11), W11530,
584 doi:10.1029/2010WR009274.

585 Mika, S., B. Schölkopf, A. J. Smola, K. R. Müller, M. Scholz, and G. Rätsch (1999),
586 Kernel PCA and de-noising in feature spaces, *Advances in neural information processing*
587 *systems*, *11*(1), 536–542.

588 Neuman, S. P. (1973), Calibration of distributed parameter groundwater flow models
589 viewed as a multiple-objective decision process under uncertainty, *Water Resources*
590 *Research*, *9*(4), 1006–1021.

591 Oliver, D. S., L. B. Cunha, and A. C. Reynolds (1997), Markov chain Monte Carlo methods
592 for conditioning a permeability field to pressure data, *Mathematical Geology*, *29*(1), 61–
593 91.

594 RamaRao, B., A. LaVenue, G. De Marsily, and M. Marietta (1995), Pilot point methodol-
595 ogy for automated calibration of an ensemble of conditionally simulated transmissivity
596 fields 1. Theory and computational experiments, *Water Resources Research*, *31*(3),
597 475–493.

598 Rubin, Y., X. Chen, H. Murakami, and M. Hahn (2010), A Bayesian approach for inverse
599 modeling, data assimilation, and conditional simulation of spatial random fields, *Water*
600 *Resources Research*, *46*, W10523, doi:10.1029/2009WR008799.

601 Salamon, P., D. Fernández-García, and J. Gómez-Hernández (2006), A review and numer-
602 ical assessment of the random walk particle tracking method, *Journal of Contaminant*
603 *Hydrology*, *87*(3-4), 277–305, doi:10.1016/j.jconhyd.2006.05.005.

- 604 Strebelle, S. (2002), Conditional simulation of complex geological structures using
605 multiple-point statistics, *Mathematical Geology*, *34*(1), 1–21.
- 606 Suzuki, S., and J. Caers (2008), A distance-based prior model parameterization for con-
607 straining solutions of spatial inverse problems, *Mathematical Geosciences*, *40*(4), 445–
608 469, doi:10.1007/s11004-008-9154-8.
- 609 Wen, X. H., J. E. Capilla, C. V. Deutsch, J. J. Gómez-Hernández, and A. S. Cullick
610 (1999), A program to create permeability fields that honor single-phase flow rate and
611 pressure data, *Computers & Geosciences*, *25*(3), 217–230.
- 612 Zhang, T., P. Switzer, and A. Journel (2006), Filter-based classification of training image
613 patterns for spatial simulation, *Mathematical geology*, *38*(1), 63–80, doi:10.1007/s11004-
614 005-9004-x.
- 615 Zhou, H., J. J. Gómez-Hernández, H.-J. Hendricks Franssen, and L. Li (2011),
616 An approach to handling Non-Gaussianity of parameters and state variables
617 in ensemble Kalman filter, *Advances in Water Resources*, *34*(7), 844–864, doi:
618 10.1016/j.advwatres.2011.04.014.

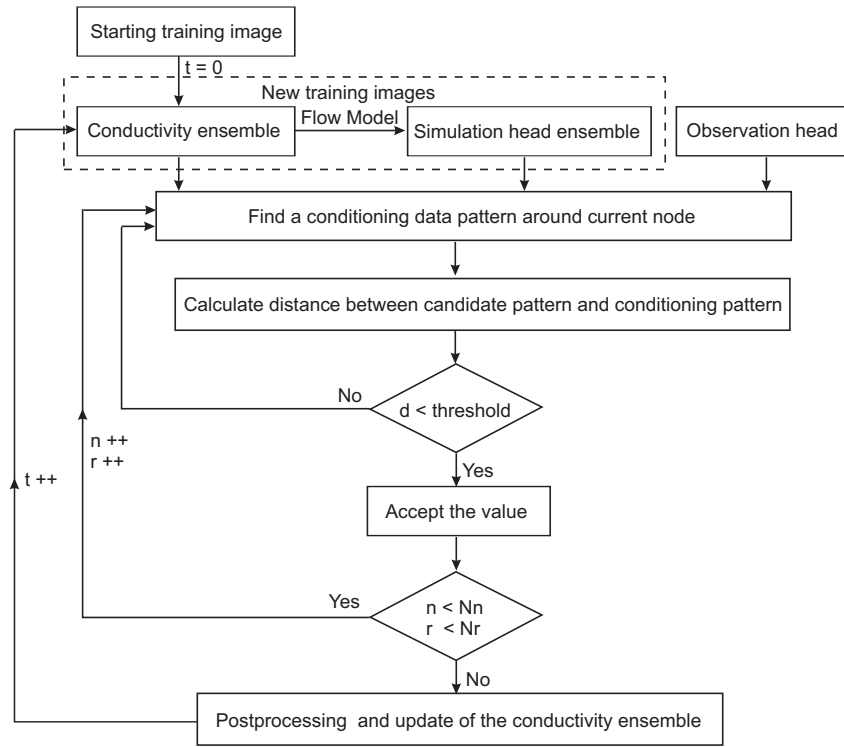


Figure 1. Flow chart of the proposed pattern searching-based multiple-point ensemble inverse method. d is the distance function value, N_n is the number of grids in each realization and N_r is the number of realizations.

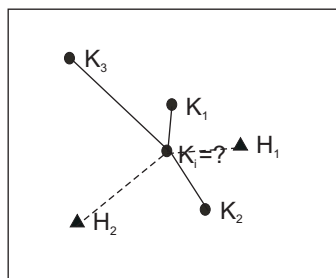


Figure 2. A pattern example consisting of conditional hydraulic conductivity and head data. K_i is the value to be simulated.

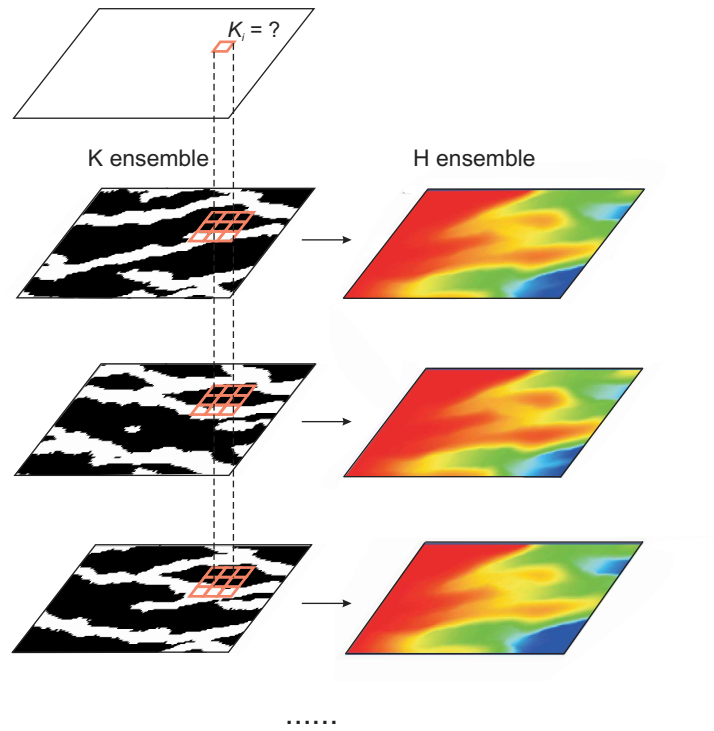


Figure 3. Sketch map of the searching strategy. The dashed line indicates the exact location of K_i through the ensemble. The candidates in the 3 by 3 square in each realization are evaluated to find the match consistent with the conditioning hydraulic conductivities and observed piezometric heads.

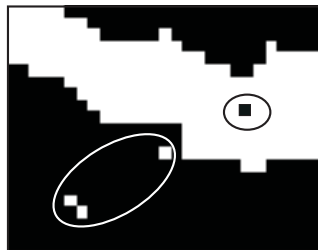


Figure 4. Sketch of filtering out noise. The black/white cells are converted to white/black so as to be consistent with the values in the neighborhood.

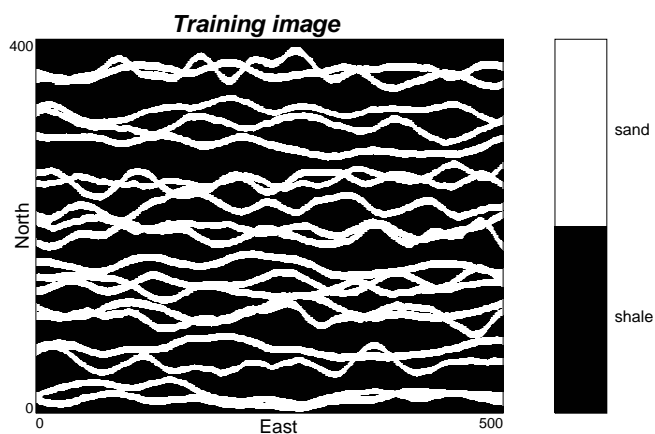


Figure 5. Training image used to generate the ensemble of binary facies realizations.

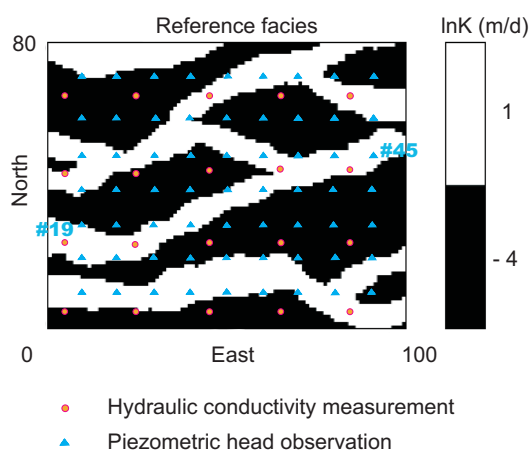


Figure 6. Reference facies field.

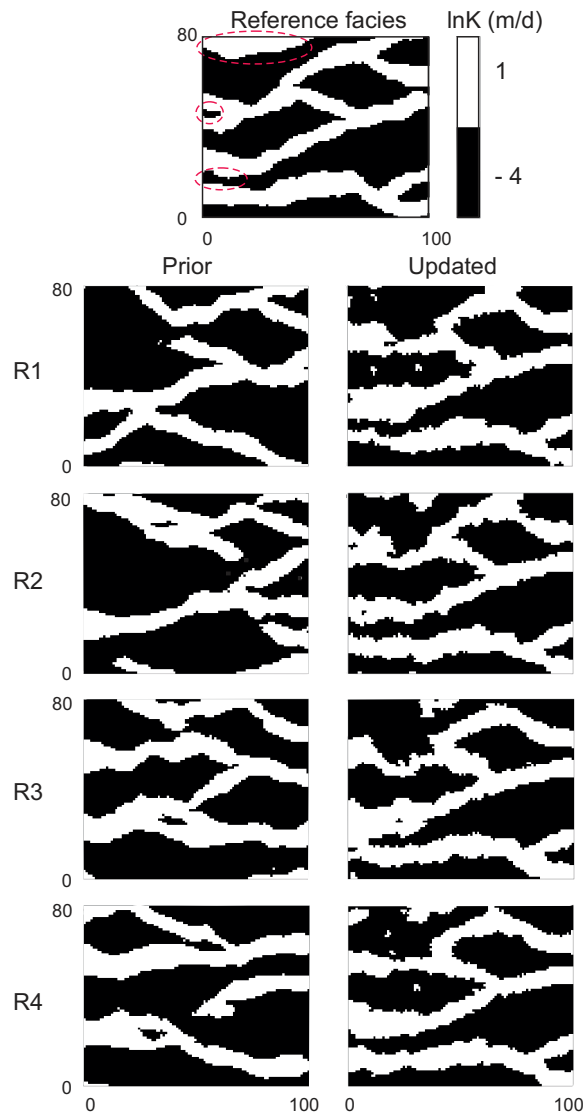


Figure 7. The first four realizations in the ensemble. The left column shows four prior facies fields and the right column shows the corresponding updated facies. The reference field is also shown for comparison.

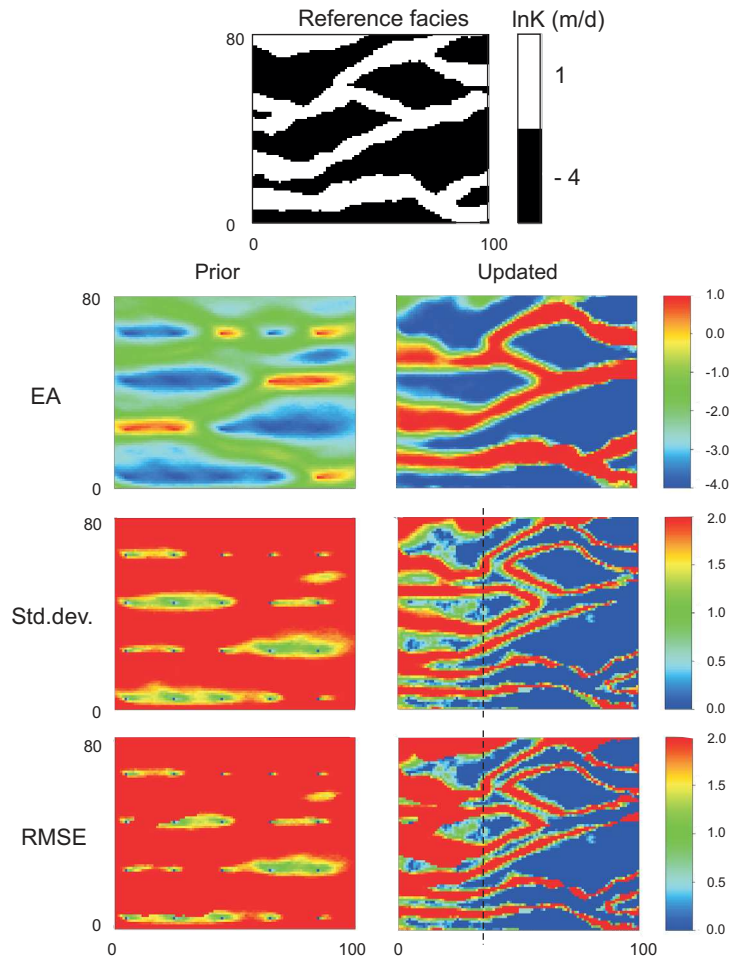


Figure 8. Ensemble average (the second row), standard deviation (the third row) and $RMSE$ (the bottom row) of $\ln K$ over the ensemble before and after head data conditioning. The reference field (the top row) is also shown for comparison.

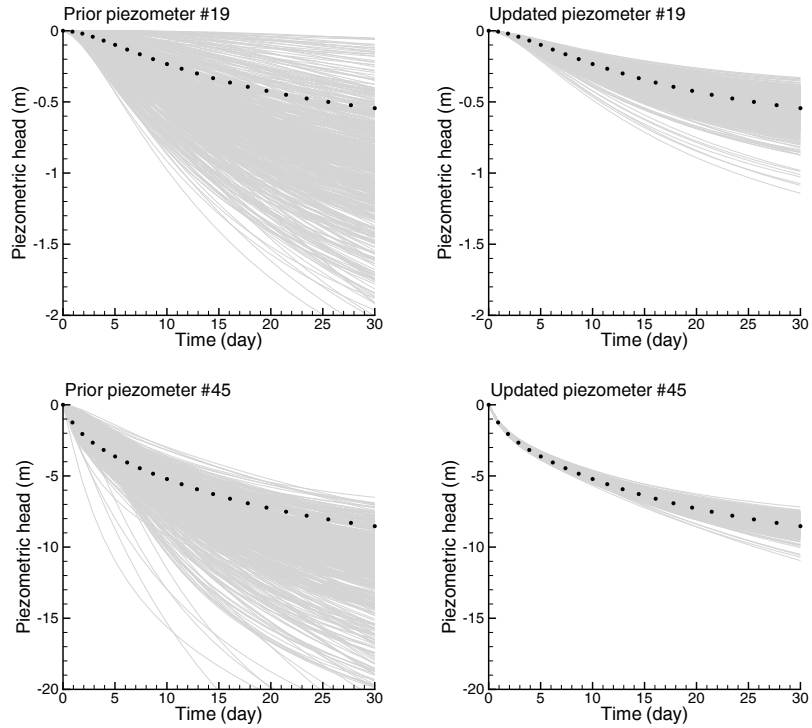


Figure 9. Piezometric head evolution at two conditioning piezometers, positions of which are shown in Figure 6. Results are shown for the prior ensemble and the updated ensemble. The dots represent the piezometric head in the reference field.

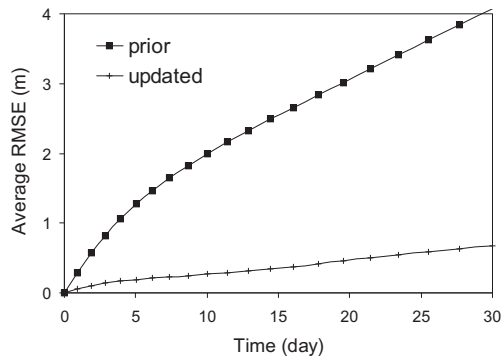


Figure 10. Evolution of average *RMSE* of piezometric heads over the field.

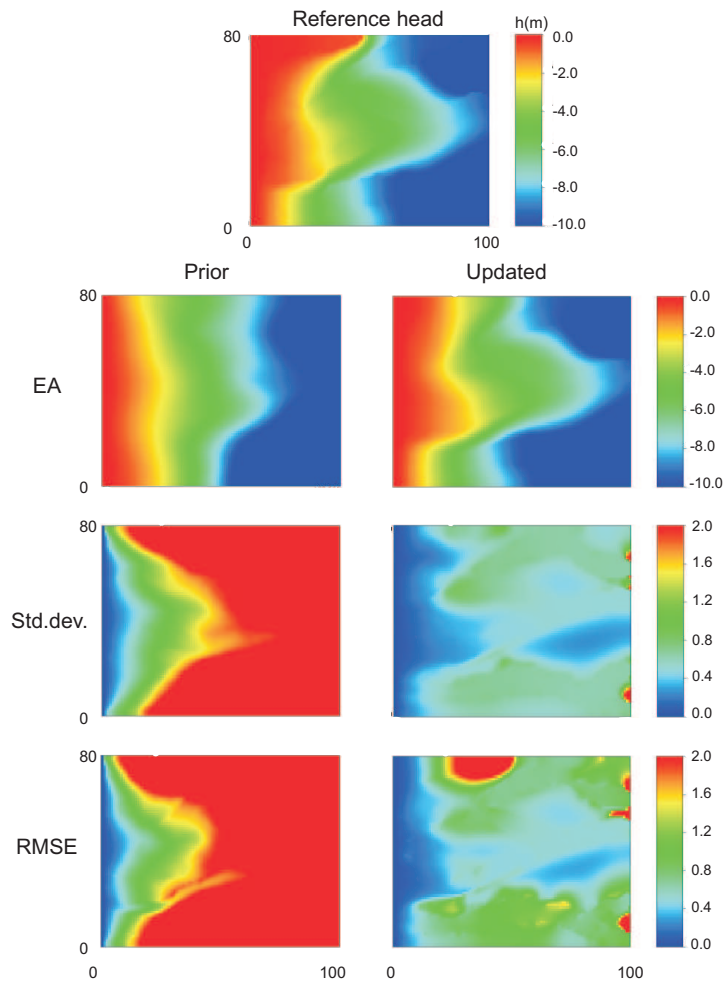


Figure 11. Ensemble average (the second row), Standard deviation (the third row) and *RMSE* (the bottom row) of hydraulic head over the ensemble before and after head data conditioning. Reference head field (the top row) is also shown for comparison.

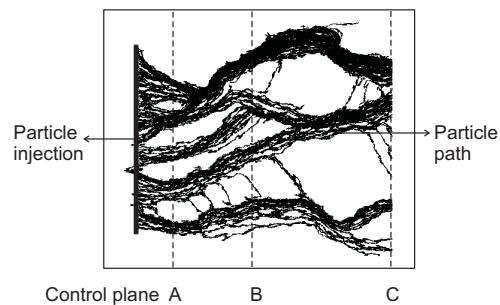


Figure 12. Configuration of the transport prediction experiment.

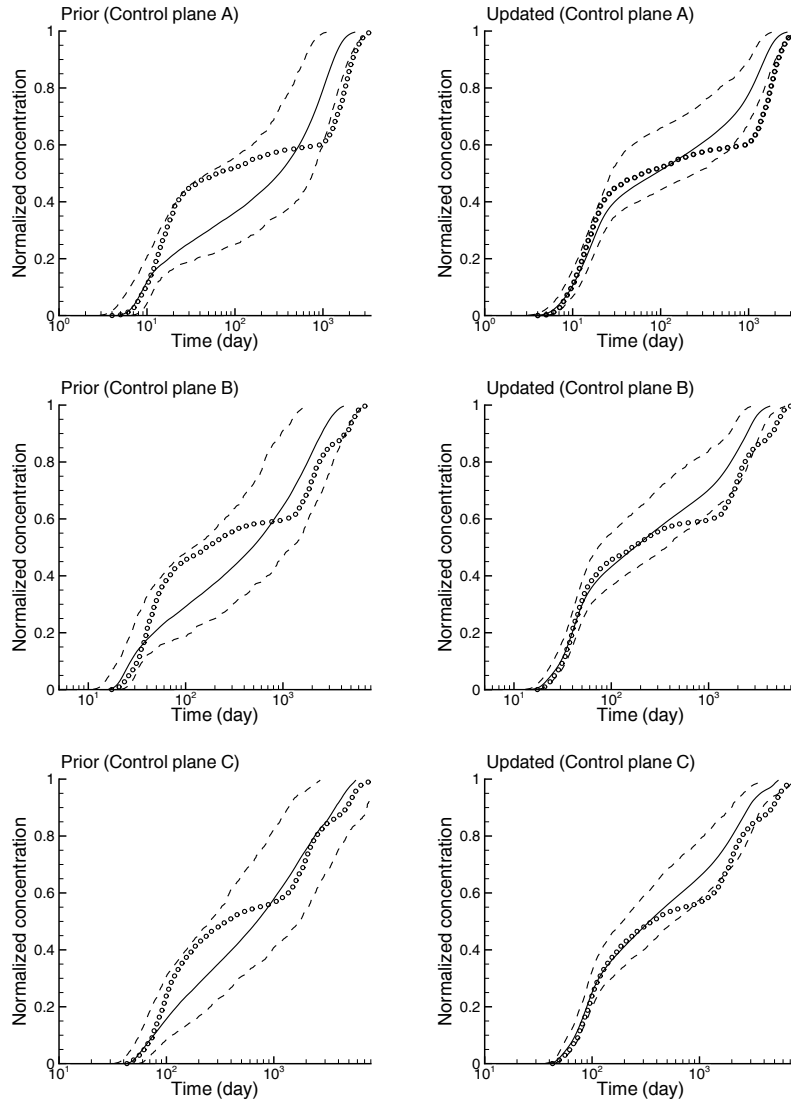


Figure 13. Summary of the breakthrough curves. The 5th percentile, the median, and the 95th percentile of the travel times are computed as a function of normalized concentration. Dashed lines correspond to the 5th and 95th percentiles, the solid line corresponds to the median, and the dotted line is the breakthrough curve in the reference. Results are shown for the prior ensemble and the updated ensemble.

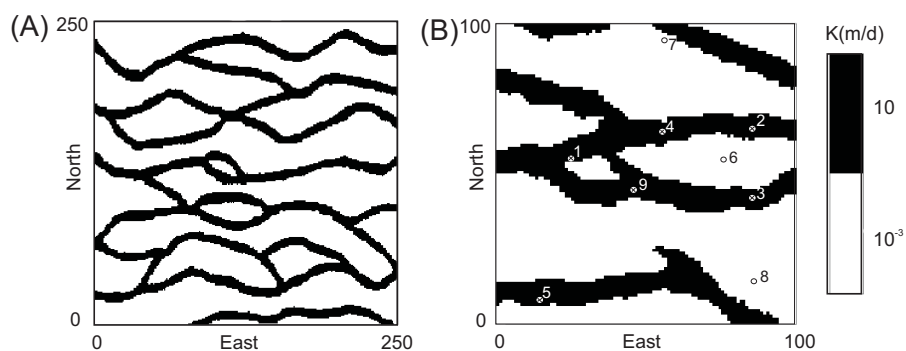


Figure 14. Training image and reference field. (A) Training image [Strebelle, 2002]. (B) Reference hydraulic conductivity field, in which the conductivities are measured at the 9 points serving as the hard data to generate the prior model and the piezometric head data at these wells are used to calibrate the prior model.

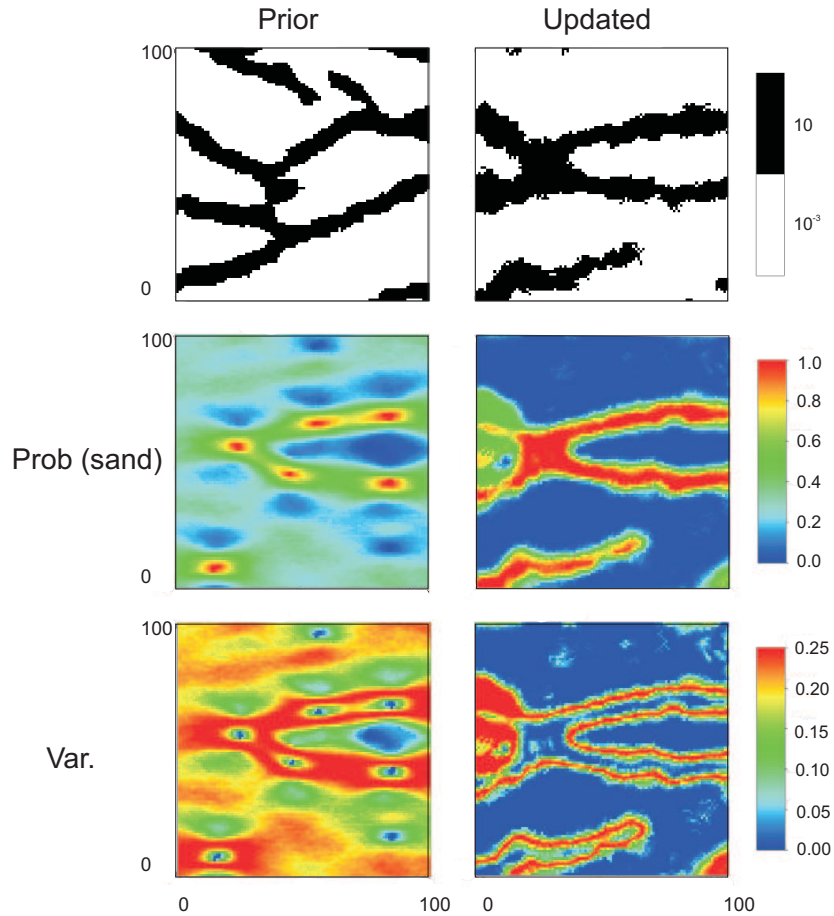


Figure 15. Comparison of the prior and calibrated hydraulic conductivity model. A realization of the ensemble (the first row), probability of being sand (the second row) and variance (the third row).

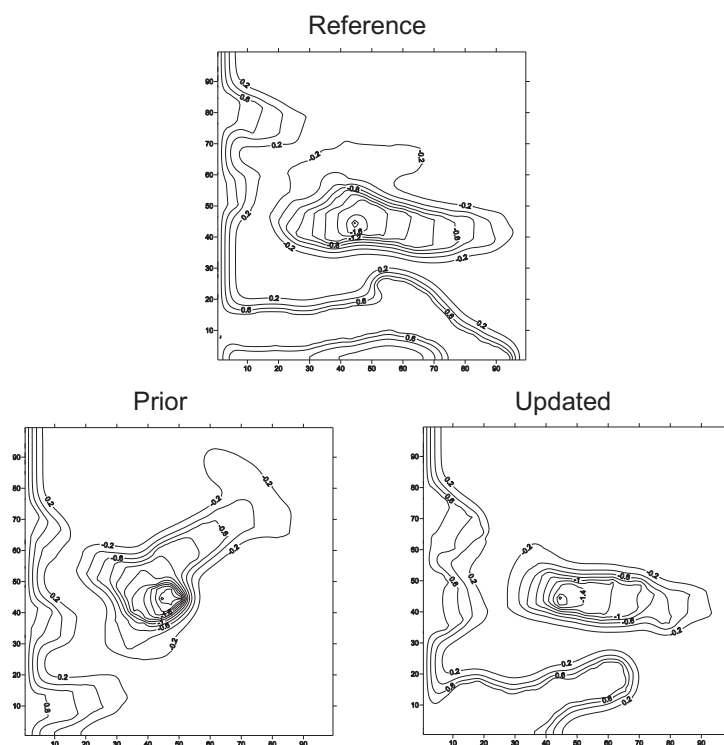


Figure 16. Hydraulic head at the end of simulation period in the reference field, prior model and updated model. Only one sample of the realization stack is shown. Hydraulic prediction uncertainty is assessed in the following figure.

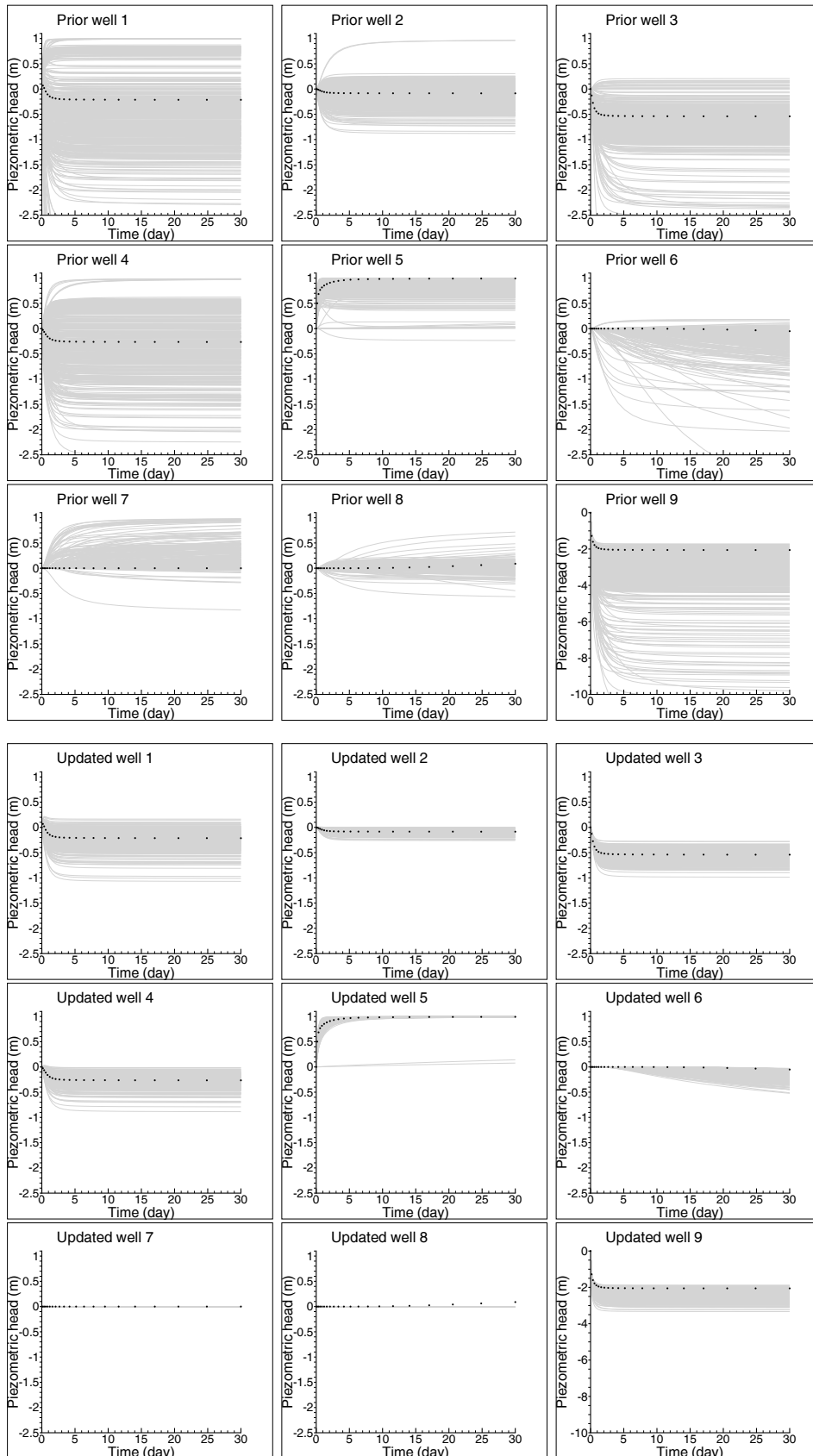


Figure 17. Piezometric head evolution at the 9 conditioning piezometers, the positions of which are shown in Figure 14B. Results are shown for the prior ensemble (the first 9 plots) and the corresponding updated ensemble (the second 9). The dotted lines represent the piezometric head in the reference. Only the first 6 days were used as conditioning data.

D R A F T

November 1, 2011, 2:38pm

D R A F T